Oxygen Carrier and Alkali Interaction in Chemical Looping Combustion: Case Study Using a Braunite Mn Ore and Charcoal Impregnated with

energy&fuels

pubs.acs.org/EF

Article

Oxygen Carrier and Alkali Interaction in Chemical Looping Combustion: Case Study Using a Braunite Mn Ore and Charcoal Impregnated with K_2CO_3 or Na_2CO_3

Daofeng Mei,* Anders Lyngfelt, Henrik Leion, Carl Linderholm, and Tobias Mattisson

Cite This: https://doi.org/10.1021/acs.energyfuels.2c00553

Read Online

ACCESS | Metrics & More | Article Recommendations

ABSTRACT: Alkali is a problematic component in biomass and may create various operation issues in normal combustion as well as chemical looping combustion using biomass fuels (bio-CLC). To investigate the interaction of alkali with an oxygen carrier, a methodology has been developed where alkali salts are added with impregnated charcoal particles. This work studies the effect of K_2CO_3 and Na_2CO_3 on the fluidization/agglomeration behavior and reactivity as well as the interaction of a braunite manganese ore oxygen carrier with K and Na in a batch fluidized bed reactor. Charcoal impregnated with K_2CO_3 (K-charcoal) and charcoal impregnated with Na_2CO_3 (Na-charcoal) were used as solid fuels in the reduction step of the simulated CLC cycles. CH_4 and syngas (50% CO + 50% H_2) were periodically used to evaluate the reactivity of braunite before and after solid fuel experiments. In total, more than 50 cycles were performed for both K-charcoal series and Na-charcoal series tests, while some additional cycles with non-impregnated charcoal were conducted and considered as a reference. Partial agglomeration and partial defluidization were found after cycles with K-charcoal and Na-charcoal, and the use of K-charcoal tends to lead to the partial agglomeration/defluidization faster than the use of Na-charcoal. K, Na, Si, and Ca were found at a higher concentration on the surface of the agglomerated particles and can be assumed to be responsible for the partial agglomeration. The partial agglomeration with K-charcoal happened likely as a result of surface melting of the braunite particles, whereas the formation of the low-melting-point Na−Si−Ca system could be responsible for agglomeration in the Na-charcoal experiments. The concentration of K and Na in the braunite bed was found to increase during cycles with the alkali charcoals. In total, the added masses of K and Na were 0.8 and 1.2% of the bed, and around 40 and 80% of added K and Na were found, respectively, in the used oxygen carrier particles. Although partial agglomeration and accumulation were observed in the presence of these alkalis, the reactivity of used braunite was scarcely changed in comparison to the fresh sample.

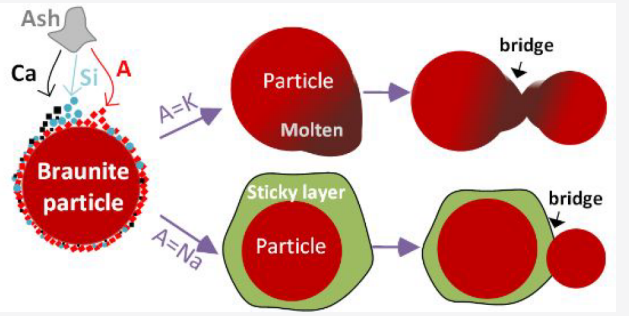

1. INTRODUCTION

Anthropogenic activities generate vast amounts of CO_2 emissions to the atmosphere and cause global warming. Mitigation of CO_2 emissions is crucial to limit the global temperature increase to a reasonable level compared to the pre-industrial period.[1] One way to mitigate CO_2 emissions is carbon capture and storage (CCS), which captures CO_2 from combustion flue gases and stores CO_2 into proper geological formations.[2,3] Several CCS technologies are under development, e.g., pre-combustion, post-combustion, and oxy-fuel combustion capture.[4] There are both advantages and disadvantages in these technologies, mainly related to the energy penalty for gas separation and system efficiencies.[5] In contrast to these technologies, chemical looping combustion (CLC)[6,7] has the advantage of inherently capturing CO_2 without a high energy penalty[8,9] and, thus, offers a promising technology for a low-carbon future.

A simplified CLC system is composed of a fuel reactor, an air reactor, and an oxygen carrier circulating between the reactors,[6,10] as seen in Figure 1. The oxygen carrier is a metal oxide (here, MeO_x represents the oxidized form, and MeO_{x-1} represents the reduced form), which is comprised of an active part (Fe, Mn, Cu, Ni, etc.) and, in the case of manufactured materials, may also include an inert support (Al_2O_3, $MgAl_2O_4$, SiO_2, ZrO_2, etc.).[11,12] Manufactured materials, naturally occurred ores (iron ore, ilmenite, manganese ore, etc.), and industrial byproducts (redmud, steel slag, etc.) have been tested

Special Issue: 2022 Pioneers in Energy Research: Anders Lyngfelt

Received: February 28, 2022
Revised: May 14, 2022

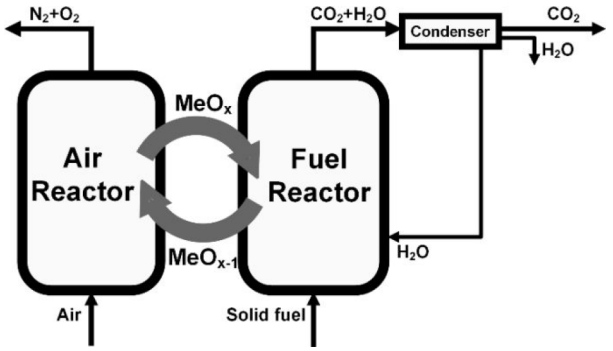

Figure 1. Schematic description of the CLC process.

in CLC systems.[7,13] Among these materials, natural ores are widely studied worldwide as a result of their low cost and being environmentally benign. Various gaseous, liquid, and solid fuels have been successfully demonstrated in the CLC process.[7,14−16] In the case of solid fuel, it is pyrolyzed to char and volatiles in the fuel reactor via reaction R1. The char is then gasified to CO and H_2 by H_2O at a high temperature (800−1000 °C) through reaction R2. Gasification products (CO and H_2) together with volatiles (e.g., CH_4, CO, H_2, etc.) react with MeO_x via reactions R3−R5, while the oxygen carrier is reduced to MeO_{x-1}. Alternatively, the fuel can also be converted with gaseous O_2 in the chemical looping with oxygen uncoupling (CLOU) process.[17] CLOU is another important CLC technology under development[18,19] and is not the focus of this work. The reduced oxygen carrier from the fuel reactor is then circulated to the air reactor and oxidized back to MeO_x through reaction R6, ready for the next cycle. By the circulation of the oxygen carrier, a CO_2 stream can be inherently generated from the fuel reactor after simple steam condensation, avoiding any intensive gas separation, making CLC a CO_2 capture technology with a low energy penalty. Use of biomass makes CLC even more attractive in view of the rapidly diminishing carbon budget for the target of a maximum 1.5 °C temperature rise,[1] because CO_2 will be captured from the atmosphere through a bio-CLC process and negative CO_2 emissions will be attained.[20,21] Demonstration of bio-CLC has been successfully performed in 0.5−100 kW_{th} pilot units[22−28] for CLC and even partial CLC in a 12 MW_{th} boiler,[29] and more research is needed for bio-CLC.

$$\text{solid fuel} \rightarrow \text{char} + \text{volatiles } (CH_4, CO, \text{and } H_2) \quad \text{(R1)}$$

$$\text{char} + H_2O \rightarrow CO + H_2 + \text{ash} \quad \text{(R2)}$$

$$CH_4 + MeO_x \rightarrow CO_2 + H_2O + MeO_{x-1} \quad \text{(R3)}$$

$$CO + MeO_x \rightarrow CO_2 + MeO_{x-1} \quad \text{(R4)}$$

$$H_2 + MeO_x \rightarrow H_2O + MeO_{x-1} \quad \text{(R5)}$$

$$MeO_{x-1} + \text{air} \rightarrow MeO_x + N_2 + O_2 \quad \text{(R6)}$$

Ash from solid fuels is incombustible in CLC, and it is the main residue in the fuel reactor after the devolatilization of fuel and gasification of char (see reaction R2). In a large-scale CLC system, the ash will need to be removed from the reactor system to avoid accumulation and potential operational problems.[30−32] When using biomass in bio-CLC, the effect of fuel ash requires attention, because alkalis (K and Na) in biomass, especially herbaceous biomass, are present in a much higher proportion compared to coal ash.[33] In a gasification process, these alkalis can catalyze the char gasification and, thus, result in faster biomass conversion.[34−36] Nevertheless, the high alkali concentration is also a main reason for bed agglomeration in fluidized bed combustion.[37,38] In addition, derivates from alkalis (e.g., alkali chlorine) contribute to fouling heat exchanger surfaces and reactor walls.[39,40] Alkalis in biomasses are usually present as finely dispersed salts, such as organic alkalis (ammonium-acetate-based, −OOC) and inorganic components mainly based on CO_3^{2-}, SO_4^{2-}, Cl^-, etc.[41−45] These salts are released during the thermal conversion of biomass, forming gas-phase alkalis, which later attach on the walls of heat exchangers and lower the heat transfer efficiency, and they also form acidic liquid when contacting with condensed water. As fouling and corrosion on the surfaces and walls develop, operation failures and even accidents can happen to boiler systems, in addition to affecting the heat-transferring process.

Effects of corrosion and fouling from alkali will be different in the CLC process compared to conventional combustion, because the fuel conversion and most of the heat extraction will take place in different reactors.[46] This is because the oxygen carrier oxidation reaction R6 is highly exothermic. Heat transfer surfaces are placed in the air reactor,[46] while the fuel alkalis are present in the fuel reactor, where no heat exchangers are placed. This reduces the contact of alkalis with the heat transfer surfaces and, thus, lowers the risk of operation failures from corrosion and/or fouling in CLC. Nonetheless, the oxygen carrier is in direct contact with ash in the fuel reactor, and this may lead to oxygen carrier and ash interactions that are both advantageous and disadvantageous for CLC operation. Impregnation of K^+ or Na^+ in an ilmenite oxygen carrier has greatly promoted the reduction activity of ilmenite with CO.[47] This promotion might be attributed to the development of pores in the particles, migration of K and Na ions, and/or formation of more reactive new phases in ilmenite. Using an iron ore, the effect of coal ash components on the reactivity of the oxygen carrier was also explored.[48,49] An increase of Ca was also found to have a positive effect on oxygen carrier reactivity. It seems that the reactivity of the oxygen carrier depends a lot upon the type of alkali and oxygen carrier.[50,51] Apart from the reactivity, the fluidization and agglomeration behaviors[52] with the presence of alkali are another important issue in the bio-CLC process. Alkali species with low melting points are usually considered responsible for gluing/sticking bed particles together, causing agglomerations in conventional fluidized bed fuel conversion.[53] Among various alkaline salts (KCl, KH_2PO_4, K_2CO_3, and K_2SO_4) investigated,[50,54] KH_2PO_4 seems to have the highest tendency to form bed agglomeration with ilmenite, Linz−Donawitz (LD) slag, and iron mill scale oxygen carriers. In addition, K_2O-SiO_2 and $CaO-K_2O-SiO_2$ slags or melts were also considered responsible for the bed agglomeration in the biomass-based CLC process.[55] In operation of CLC pilot units, the fate of alkalis and their presence in the gas from the air reactor and fuel reactor as well as in the oxygen carrier have been measured and evaluated.[56,57] Alkali retention in the oxygen carrier material is significant, as found in 60 and 100 kW_{th} experiments.[56,57] Although there is research focusing on the effect of alkalis on ilmenite and iron ore, the interaction of alkalis with manganese ores is not so well-investigated. The effects on reactivity, fluidization behavior, and agglomeration behavior of manganese ores induced by the exposure to an alkali-containing reacting environment deserve further study.

This work studies the interaction of K and Na alkalis with a braunite manganese ore in a batch fluidized bed reactor. Alkali salts (K_2CO_3 and Na_2CO_3) were impregnated in charcoal

https://doi.org/10.1021/acs.energyfuels.2c00553
Energy Fuels XXXX, XXX, XXX−XXX

particles and injected into the reactor, providing reduction steps of the cyclic oxidation/reduction tests. More than 50 cycles were conducted to explore the defluidization/agglomeration behavior induced by the interaction between the alkalis and the oxygen carrier. Reactivity of the bed material was regularly checked after middle and final cycles with K-charcoal and Na-charcoal. The composition and microstructure of the fresh oxygen carrier and middle and final samples were analyzed by different characterization techniques.

2. EXPERIMENTAL SECTION

2.1. Characterization Techniques. Crystal-phase composition of the oxygen carrier was analyzed by the X-ray diffraction (XRD) technique (Bruker D8 Advance). The scanning was carried out from 10° to 90° at a step size of 2θ = 0.3°/s using Cu Kα radiation with a generator setting of 40 mA and 40 kV. Proximate and ultimate analyses of solid fuels were performed following several International Organization for Standardization (ISO) standard methods.[58−63,63] The moisture, ash, and volatile matter were analyzed with a Leco TGA-701 analyzer. Sulfur was analyzed using an Eltra Helios analyzer, while carbon, hydrogen, and nitrogen were analyzed by a Leco CHN-628 analyzer. Metal elements in the solid fuel and oxygen carrier particles were determined using the inductively coupled plasma optical emission spectrometry (ICP−OES) technique (PerkinElmer Optima 8300) following a modified ASTM D3682 method.[64] Morphology of the oxygen carrier samples was studied using a light microscope (MICRO-80150, TAGARNO), while the microstructure was subject to scanning electron microscopy−energy-dispersive X-ray spectroscopy (SEM−EDX) analysis (JEOL JSM-7800F Prime). To study the cross-section of the particles, some samples were dispersed in epoxy resin, modulated, cut, and polished to expose the cross-section part and used in the SEM−EDX characterization.

2.2. Braunite Manganese Ore Oxygen Carrier. Here, braunite does not refer to the mineral but the name used by the supplier for one of their manganese ores. Like most manganese ores, it contains manganese, iron, and silicon as the main constitutes. Braunite was from the same batch as that used in a 60 kW_{th} continuous unit for CLC operations.[57,65] Before the experiments, braunite was calcined at 500 °C for 1 h and 950 °C for 12 h to strengthen the particles and then sieved to 0.1−0.3 mm. As shown in Table 1, fresh calcined braunite has 52.0% Mn, 11.0% Fe, 2.6% Si, and 2.5% Ca as the main components, while the alkalis (K and Na) are less than 0.3%, which is low and suitable for this study; i.e., the effect of alkalis originating from braunite is negligible.

Table 1. Main Chemical Composition of the Braunite Samples, Determined by the ICP−OES Technique (wt %, Dry Basis)[a]

	Mn	Fe	Si	Ca	K	Na
fresh	52.0	11.0	2.6	2.5	0.22	0.29
K-middle	49.0	11.0	3.1	2.3	0.22	0.16
Na-middle	53.0	11.0	2.6	2.6	0.26	0.65
K-final	48.0	11.0	4.3	2.3	0.69	0.23
Na-final	52.0	11.0	3.3	2.5	0.18	0.91

[a]Fresh means fresh braunite before any tests, and K-middle, Na-middle, K-final, and Na-final refer the samples taken from the middle and final cycles (cf. Figure 5 below) of operation with K-charcoal and Na-charcoal.

Phase composition of the braunite samples was identified by comparing the acquired XRD patterns to the Inorganic Crystal Structure Database (ICSD).[66] As seen in Figure 2, fresh braunite is mainly composed of bixbyite [$(Mn,Fe)_2O_3$], which is a compound having the capability of releasing gaseous oxygen,[67] known as the CLOU property.[17,68,69] Previous work with braunite shows that bixbyite releases oxygen.[70] Some hausmannite [$Mn(Mn,Fe)_2O_4$] was also identified in fresh braunite, and this is not capable of releasing gaseous oxygen. Si- and Ca-based components were not identified from the XRD analysis of fresh braunite, although they were detected by ICP−OES analysis. This might be because of their low concentration or presence in amorphous forms. The oxygen carrier samples used with K-charcoal and Na-charcoal, i.e., K-final and Na-final, will be discussed later in this work.

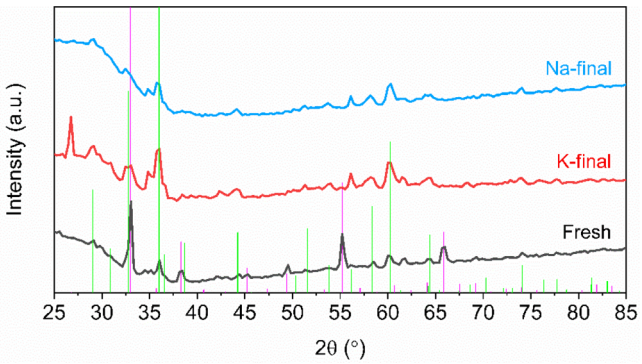

Figure 2. Identification of phase composition from XRD patterns of fresh, K-final, and Na-final braunite. Standard peak positions of bixbyite $(Mn,Fe)_2O_3$ are shown with vertical pink lines, and standard peak positions of hausmannite $Mn(Mn,Fe)_2O_4$ are shown with vertical green lines. The peak at 2θ = 26.8° for K-final might correspond to SiO_2. Patterns in the range of 2θ = 10−25° and 85−90° were considered as noises and are not shown.

2.3. Fuels. *2.3.1. Gaseous Fuels.* The reactivity of fresh and used braunite samples was studied using CH_4 and syngas (50% CO + 50% H_2) in a batch fluidized bed reactor, as described in section 2.4 below. These gases are major components in volatiles from biomass and were judged to be applicable here for comparison of oxygen carrier reactivity. Both CH_4 and syngas were regulated close to atmospheric pressure before use.

2.3.2. Solid Fuels. Charcoal, K-charcoal, and Na-charcoal were used as the solid fuels in this work. The "charcoal" was provided by Chemviron Carbon and has an original name of CARBSORB 30. The charcoal was in the form of granular activated carbon from the pyrolysis of a bituminous coal. To be used in this work, the charcoal was crushed and sieved to 1−1.25 mm particles, which have a porosity of approximately 0.47 mL/g. The K-charcoal and Na-charcoal were prepared by incipient dry impregnation of K_2CO_3 and Na_2CO_3 solutions in the charcoal particles. In the incipient dry impregnation, the charcoal particles were continuously heated in a glass container, which was placed on a heating plate with a temperature of around 150 °C. Solutions of 3.5 mol/L K_2CO_3 and 1.5 mol/L Na_2CO_3 were respectively impregnated in the charcoal. The K-charcoal and Na-charcoal samples were obtained after one impregnation and two successive impregnations, respectively, which theoretically correspond to a weight percentage of 10.5% K in the K-charcoal and 5.7% Na in the Na-charcoal. It is noted that carbon introduced with K_2CO_3 or Na_2CO_3 is below 1.6% of the solid fuel and, thus, has a negligible effect on the CO_2 concentration measured during the fluidized bed experiments, as described below.

Charcoal is mainly comprised of carbon and extremely low K and Na, while the K-charcoal and Na-charcoal have 8.1% K and 4.9% Na, respectively (see Table 2). Measured K and Na are less than the theoretical values (10.5 and 5.7%) as a result of losses during preparation with impregnations. The losses are likely caused by part of the alkali solution attaching to the surface of the glass container instead of the particle surface. Ash and volatile fractions of K-charcoal and Na-charcoal both increased in comparison to charcoal. On the one hand, the impregnation directly increased the amount of ash in the form of K- and Na-based species.[59] On the other hand, the decomposition of K_2CO_3 and Na_2CO_3 during the analysis of the volatile content[60] contributes to a higher percentage of volatiles than charcoal. Around 2.0−2.7% Si was also measured in charcoal, K-charcoal, and Na-charcoal.

https://doi.org/10.1021/acs.energyfuels.2c00553
Energy Fuels XXXX, XXX, XXX−XXX

Table 2. Composition of Charcoal, K-Charcoal, and Na-Charcoal

	proximate (wt %, ar)				ultimate (wt %, ad)				metals (wt %, ad)		
	FC	V	M	A	C	H	S	N	Si	K	Na
charcoal	84.3	4.9	1.9	8.9	89.0	<0.3	0.7	0.45	2.7	0.05	0.03
K-charcoal	53.0	15.7	3.3	28	73.0	<0.3	0.4	0.36	2.0	8.1	0.04
Na-charcoal	62.2	14.7	3.1	20	80.0	<0.3	0.9	0.42	2.4	0.03	4.9

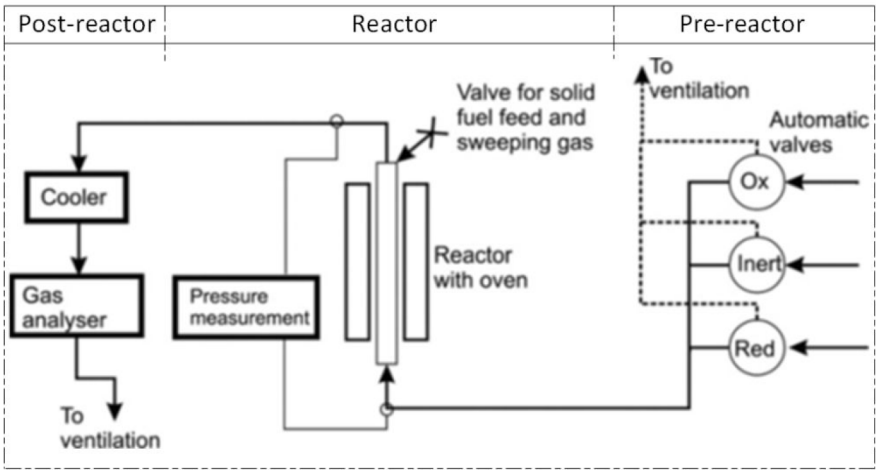

Figure 3. Batch fluidized bed reactor system.

2.4. Batch Fluidized Bed System. *2.4.1. System Setup.* The batch fluidized bed system is comprised of pre-reactor, reactor, and post-reactor parts, as seen in Figure 3. In the pre-reactor part, three magnetic valves were used to control the reacting gas environment in the reactor tube. The gas can be set to oxidation, inert, and reduction, corresponding to "ox", "inert", and "red", respectively. When one of the three channels is open, the other two are automatically switched to ventilation. Cycles for oxidation, inert, and reduction were realized by periodically changing among "ox", "inert", and "red" using a computer program. The reactor part has a conical-shape quartz tube, which is detailed in section 2.4.2 below and an electrical high-temperature oven. The temperature in the reactor was monitored by upper and lower thermal couples, located at 20 mm above and 10 mm below the gas distributor, respectively. The readings from the upper thermal couple are referred to the reactor temperature in this work. On top of the quartz tube, a valve was used for solid fuel injection, which, at the same time, allows for a sweep N_2 gas stream to pass over the fuel, facilitating injection. The pressure drop over the reactor was measured by a pressure transducer with a sampling rate of 10 Hz, and the pressure fluctuation was used to study the fluidization state. In the post-reactor part, gas from the reactor was sequentially led to a condenser to remove steam and to a gas analyzer (NGA 2000, Rosemount) to measure the concentrations of CH_4, CO, CO_2, H_2, and O_2. Simultaneously, the gas analyzer measured the total volumetric flow rate of dry gas leaving the reactor. Both the gas concentration and flow rate were sampled with a rate of one data every 2 s. All of the data for the concentration, flow rate, temperature, and pressure drop were collected by a logger connected to a computer.

2.4.2. Conical-Shape Reactor Tube. As shown in Figure 4, a quartz tube having a total length of 870 mm was used in this work as the reactor. At about 370 mm from the tube bottom, there is a quartz porous plate serving as a gas distributor. The quartz tube was conically shaped just above the gas distributor to enhance mixing in the bed. Below the gas distributor, the tube has an inner diameter of 10 mm, which increases to 30 mm at around 20 mm from the plate. This 30 mm inner diameter is kept constant for around 250 mm and then further increased to 45 mm at another 20 mm from the top of the 250 mm part. The 45 mm inner diameter is maintained for an additional 100 mm. Finally, the tube inner diameter is reduced to 30 mm after another 20 mm length. This disengaging upper section of the reactor is designed to avoid small fuel and bed particles from leaving the reactor. In addition, quartz wool was place on the tube top to prevent the bed and fuel particles from leaving the reactor.

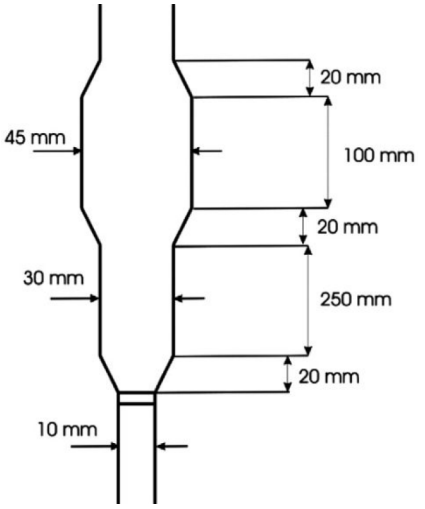

Figure 4. Conically shaped quartz reactor tube.

2.4.3. Experimental Procedure. The reduction and oxidation steps in CLC were simulated by alternatingly exposing braunite to a fuel-containing environment (CH_4, syngas, charcoal, K-charcoal, or Na-charcoal) and an oxidizing environment at a reaction temperature of 950 °C. The oxidation period usually takes around 420 s in a 4.5% O_2 + 94.5% N_2 mixture with a flow rate of 900 mL/min, giving a velocity falling from 0.8 to 0.1 m/s in the first 20 mm at 950 °C, and the condition in the reduction period varied depending upon the fuel used, as seen below.

2.4.3.1. Two Series of Alkali Experiments. Starting from room temperature, the bed was heated in N_2 flow until reaching 950 °C. Before any cycle with solid fuel, a 20 g fresh braunite bed was reacted with CH_4 with a flow rate of 345 mL/min and velocity of 0.3 m/s at 950 °C for 20 s in reduction and 4.5% O_2 in oxidation. These initial

https://doi.org/10.1021/acs.energyfuels.2c00553
Energy Fuels XXXX, XXX, XXX−XXX

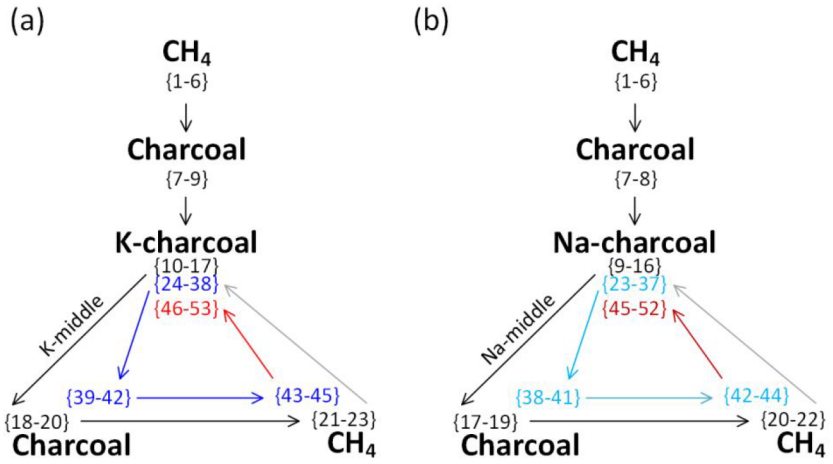

Figure 5. Two series of experiments with (a) K-charcoal and (b) Na-charcoal. The consecutive cycle numbers are presented in parentheses. Arrows show the experimental flow stream.

reactions were repeated for 6 cycles (see Figure 5) to help stabilize the braunite reactivity prior to solid fuel reactions.

Solid fuel reactions were performed using the same braunite bed after 6 cycles with CH_4, as described in Figure 5. The study of K-charcoal and Na-charcoal was carried out in two identical tubes but one used the K-charcoal experiments and the other used the Na-charcoal experiments to avoid cross-contamination. In the reduction step with solid fuels, 0.1 g of charcoal, K-charcoal, or Na-charcoal was injected to the reactor. Fluidization gas in the reduction was a mixture of 48% H_2O and 52% N_2 with a total flow rate of 865 mL/min and velocity of 0.75 m/s at 950 °C. From the fuel addition port on the reactor top, a 300 mL/min sweeping N_2 flow was maintained until the end of reduction. For the K-charcoal study, in Figure 5a, methane-stabilized braunite was first reacted with charcoal for 3 cycles, i.e., cycles 7−9, to know the char gasification behavior before any use with the alkalis. Afterward, the bed was sequentially used in 8 cycles with K-charcoal, 3 cycles with charcoal, and 3 cycles with CH_4. The reactivity of methane and non-impregnated charcoal was again evaluated to see whether K introduced previously affected the oxygen carrier in any way. The same procedure with K-charcoal, charcoal, and CH_4 was repeated for more cycles (see cycles 24−45 in Figure 5a). The series of tests for K-charcoal were finalized with another 8 cycles with K-charcoal, i.e., cycles 46−53 in Figure 5a. The same procedure was used for the Na-charcoal study, but only 2 cycles were performed with charcoal prior to the Na-charcoal, as observed in Figure 5b. In both series of experiments, the bed was sampled in the middle and final cycles and used in the characterizations, as described in section 2.1. The samples taken after cycles 17 and 53 in Figure 5a were designated as K-middle and K-final, while Na-middle and Na-final samples were collected after cycles 16 and 52 (cf. Figure 5b).

2.4.3.2. Reactivity of Braunite with CH_4 and Syngas. The reactivity of the K-final sample with CH_4 obtained from cycles 43−45 can be directly compared to that from cycles 1−6 in Figure 5a to study the effect of K-charcoal use, while the effect of using Na-charcoal on braunite can be estimated from cycles 1−6 and 42−44 in Figure 5b. The reactivity of braunite samples with syngas was evaluated with another experimental series using fresh, K-final, or Na-final braunite samples at 950 °C. A 2 g braunite sample (fresh, K-final, or Na-final) was mixed with 13 g of sand and exposed to reaction cycles with 450 mL/min syngas, and the gas velocity was 0.4 m/s at 950 °C. Braunite was diluted with sand to reach an incomplete conversion of CO and H_2 in the syngas, facilitating the data evaluation described below. For the fresh braunite sample, 6 cycles were carried out with the syngas, and for the K-final and Na-final samples, 10 cycles were made.

3. DATA EVALUATION

On the basis of the gas concentrations and oxygen balance, the mass-based oxygen carrier conversion, ω, can be calculated. For CH_4 and syngas, because different stoichiometric amounts of oxygen are needed for their full conversion to CO_2 and H_2O, the following equations (eqs 1 and 2) were used to obtain the oxygen carrier conversion:

$$\omega_{CH_4} = 1 - \int_{t_0}^{t} \frac{\dot{n}_{out} M_O}{m_{ox}} (4x_{CO_2} + 3x_{CO} - x_{H_2}) dt \quad (1)$$

$$\omega_{syn} = 1 - \int_{t_0}^{t} \frac{\dot{n}_{out} M_O}{m_{ox}} (2x_{CO_2} + x_{CO} - x_{H_2}) dt \quad (2)$$

where $\dot{n}_{out}$ is the outlet dry gas molar flow rate, obtained by applying a calibration factor on the flow readings from the gas analyzer.[71] M_O is the molar mass of atomic oxygen, and m_{ox} is the amount of braunite used in the bed; i.e., m_{ox} = 20 g for CH_4 and 2 g for syngas. Symbol x_i (i = CH_4, CO_2, CO, or H_2) represents the measured dry concentration; t_0 means the time at the beginning of reduction; and t is the instantaneous reaction time.

The gas yield, γ_i, of CH_4 and CO or H_2 in syngas represents the extent of fuel conversion in the reduction. This parameter reflects the efficiency of oxygen transfer from the oxygen carrier to the fuel gases and can be calculated through eqs 3, 4, and 5 for CH_4, CO, and H_2, respectively

$$\gamma_{CH_4,CH_4} = \frac{x_{CO_2}}{x_{CH_4} + x_{CO} + x_{CO_2}} \quad (3)$$

$$\gamma_{CO,syn} = \frac{x_{CO_2}}{x_{CO} + x_{CO_2}} \quad (4)$$

$$\gamma_{H_2,syn} = 1 - \frac{x_{H_2}}{x_{CO} + x_{CO_2}} \quad (5)$$

where total carbon at the outlet, i.e., $x_{CH_4} + x_{CO} + x_{CO_2}$ for methane and $x_{CO} + x_{CO_2}$ for CO in syngas, was used in the denominator of eqs 3 and 4. "$x_{CO} + x_{CO_2}$" in eq 5 corresponds to total H_2 because of the equal amounts of CO and H_2 in the syngas entering the reactor.

Using the gas yield obtained in eqs 3−5, the reactivity of CH_4, CO, and H_2 with braunite can be represented with rate constant k_i, calculated via eqs 6−8 below, under the assumptions of atmospheric operation pressure and first-order reaction between the fuel components and oxygen carrier

https://doi.org/10.1021/acs.energyfuels.2c00553
Energy Fuels XXXX, XXX, XXX−XXX

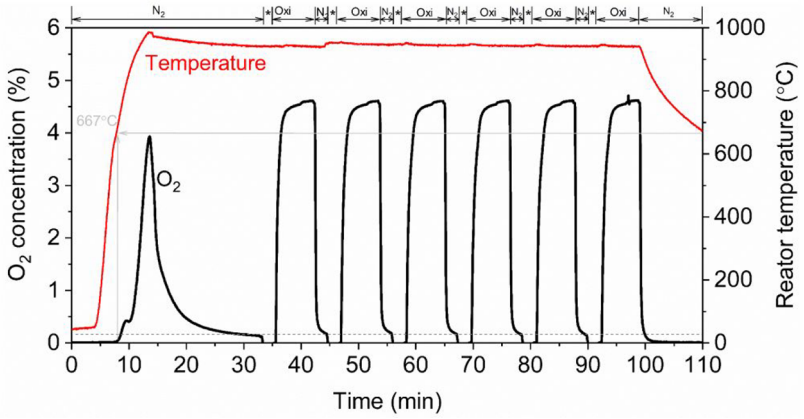

Figure 6. O_2 concentration and reactor temperature in the heating under N_2 and under cycles 1−6 with CH_4 and 4.5% O_2. The period labeled with "∗", between "N_2" and "Oxi", above the figure frame corresponds to the braunite reduction with CH_4 and the following purge with N_2.

$$k_{F,CH_4} = \frac{V_{CH_4}(-(1+\varepsilon)\ln(1-\gamma_{CH_4}) - \varepsilon\gamma_{CH_4,CH_4})}{m_{ox}} \quad (6)$$

$$k_{F,CO} = \frac{V_{syn}(-\ln(1-\gamma_{CO,syn}))}{m_{ox}} \quad (7)$$

$$k_{F,H_2} = \frac{V_{syn}(-\ln(1-\gamma_{H_2,syn}))}{m_{ox}} \quad (8)$$

where V_{CH_4} and V_{syn} are the inlet volumetric flows of CH_4 and syngas, respectively. The symbol ε is the volumetric expansion ratio for the full combustion of CH_4, and its value is 2; i.e., 1 mol of CH_4 generates 1 mol of CO_2 and 2 mol of H_2O after complete oxidation.

During solid fuel experiments, the total mass of carbon at time t, $m_C(t)$, leaving the reactor can be calculated using the concentrations of carbonaceous gases and the total outlet gas flow rate. The amount of carbon from the reactor was obtained considering only the gases from reduction

$$m_C(t) = \int_{t_0}^{t} \dot{n}_{out} M_C (x_{CH_4} + x_{CO_2} + x_{CO}) dt \quad (9)$$

where M_C is the atomic mass of the carbon atom and $\dot{n}_{out}$ is the molar gas flow passing through the gas analyzer, being corrected by calibration.

Thus, the carbon conversion from the solid fuels as a function of the reaction time, $X_C(t)$, can be easily obtained as the ratio between $m_C(t)$ and the total amount of carbon from the reactor exit, $m_{C,tot}$

$$X_C(t) = \frac{m_C(t)}{m_{C,tot}} \quad (10)$$

where $m_{C,tot}$ is the total mass of carbon measured from the reactor exit, calculated from eq 9 using the entire reduction period as the time range for integration. This is because there is negligible solid fuel left after any of the reduction periods, as confirmed by the oxidation period in each cycle.

The rate of char gasification, r_{inst}, is based on the instantaneous residual amount of carbon in the reduction period and calculated using the above obtained carbon conversion data.

$$r_{inst} = \frac{1}{1-X_C}\frac{dX_C}{dt} \quad (11)$$

The gas conversion, η_{gas}, for charcoal, K-charcoal, and Na-charcoal indicates the ratio of CO and H_2 converted to CO_2 and H_2O in the reduction and was calculated through eq 12.

$$\eta_{gas} = 1 - \frac{0.5x_{CO} + 0.5x_{H_2}}{x_{CO_2} + x_{CO}} \quad (12)$$

The fluidization state of the bed was evaluated by the amplitude of pressure drop fluctuation, σ, based on the data from the middle period of the oxidation step. This middle period was selected from a data segment without influence from steam addition and gas switching

$$\sigma = \frac{1}{N-m}\sum_{i}^{N-m}\left(\frac{1}{m}\sum_{j=i}^{i+m}(\Delta p_j - \Delta p_{avg})^2\right)^{0.5} \quad (13)$$

where i is the ith pressure drop of the total N pressure drop values that were used for calculation, m is equal to 9, which is a selected value in this work to obtain the real fluctuation values, Δp_j is the jth pressure drop value used, and Δp_{avg} is the average of all of the $m + 1$ pressure drop values. Thus, the time period analyzed is broken into many shorter periods, and the amplitude is derived as the average of the amplitude of these periods. The rationale for this way of calculating the amplitude is that changes in the average value in many cases gave highly misleading values when the amplitude was just calculated over the whole time period.

4. RESULTS AND DISCUSSION

4.1. Reaction Progresses. *4.1.1. Oxygen Release in a N_2 Environment.* As stated in section 2.4.3, fresh calcined braunite was heated in N_2 and then maintained at 950 °C for the cycles with CH_4 and 4.5% O_2. The heating in N_2 as well as N_2 purge between CH_4 and 4.5% O_2 can be used to study the gaseous O_2 release from braunite. Figure 6 shows the O_2 concentration and temperature as a function of time. During the temperature increase, O_2 appeared at around 667 °C and was followed by a peak concentration of around 4% at 986 °C, which was higher than 950 °C as a result of overheating of the oven. This shows the capability of gaseous O_2 release from fresh calcined braunite, and the oxygen release could be attributed to decomposition of Mn_2O_3, bixbyite, or other combined Mn oxides.[67] However,

https://doi.org/10.1021/acs.energyfuels.2c00553
Energy Fuels XXXX, XXX, XXX−XXX

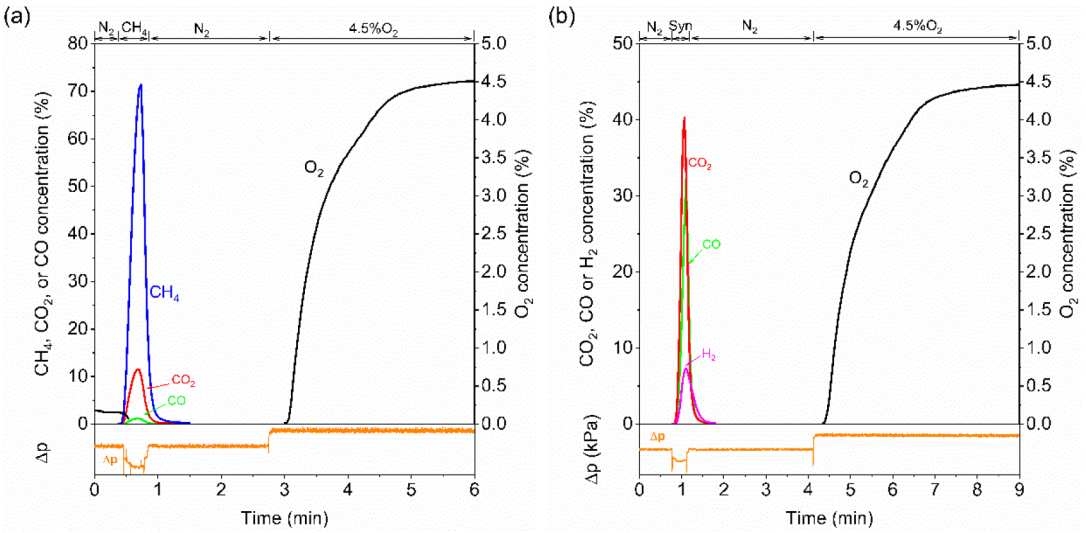

Figure 7. Concentrations of CH_4, CO, CO_2, H_2, and O_2 and pressure drop as a function of time for a typical cycle between braunite and (a) CH_4 (cycle 6 in Na series tests) and (b) syngas (cycle 5 with syngas) at 950 °C. Braunite used here has not been exposed to any cycle with K-charcoal and Na-charcoal.

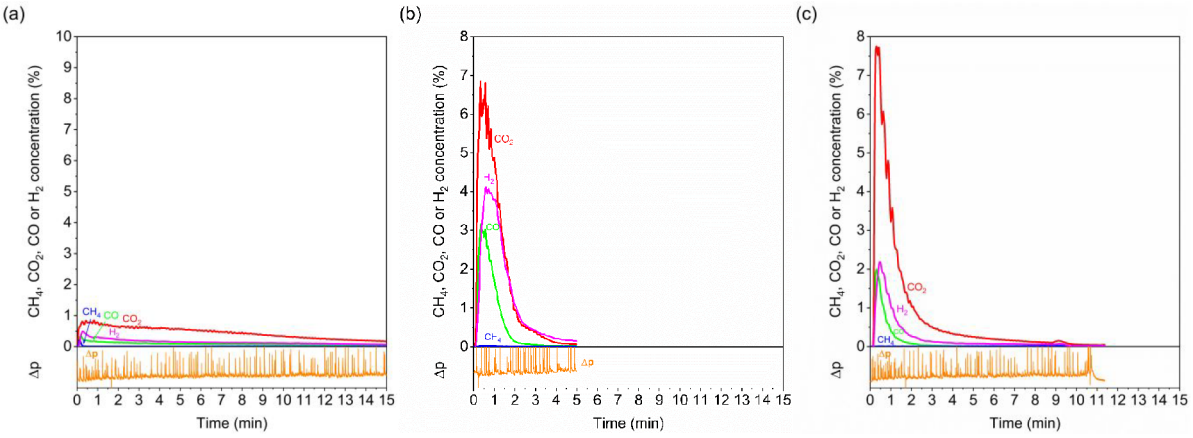

Figure 8. Concentrations of CH_4, CO, CO_2, and H_2 and pressure drop during the braunite reduction in (a) charcoal (cycle 7), (b) K-charcoal (cycle 12), and (c) Na-charcoal (cycle 12) environments at 950 °C and under the fluidization with 48% H_2O + 52% N_2.

these compounds cannot be recovered in the oxidation period[72] and actually shifted to hausmannite $Mn(Mn,Fe)_2O_4$, as indicated in Figure 2. Thus, after the peak concentration, O_2 decreased gradually to around 0.25% at around 25 min. Subsequently, the 6 cycles composed of 20 s with CH_4, 420 s with 4.5% O_2, and 120 s N_2 purge were performed, with the N_2 purge and oxidation periods being labeled as "N_2" and "Oxi" in Figure 6. The measured O_2 concentration in the "N_2" period was only around 0.25%, as shown by the horizontal dashed line for all 6 cycles, and this shows a small oxygen release from braunite. In this case, the gaseous O_2 release likely has a small impact on the reactions with gaseous fuels (CH_4, CO, and H_2), encouraging the use of a first-order reaction constant, as assumed in eqs 6−8 above.

4.1.2. Reaction with CH_4 and Syngas. Figure 7 shows a typical cycle composed of reduction with CH_4 or syngas ("CH_4" or "Syn"), inert ("N_2"), and oxidation ("4.5% O_2") for the oxygen carrier not yet exposed to any alkali. More than 70% CH_4 was not converted, and the peak concentrations of CO_2 and CO are only 11.5 and 1.1%, respectively, indicating a low reactivity of braunite with CH_4. Although significant proportions of CH_4 were not converted, carbon deposition was not seen, because no carbonaceous gas was detected in the following oxidation. The reaction with syngas showed higher reactivity, and higher conversions of both CO and H_2 in syngas were reached; i.e., residual CO is at around 30%, while H_2 is less than 7%. In comparison to CH_4, the oxidation of reduced braunite with syngas took a longer time to reach a stable O_2 concentration, because the oxygen carrier was more reduced by syngas. As seen in the lower panel of Figure 7, the reduction, inert, and oxidation steps in the cycle are well-captured by the pressure drop variation, which is a result of gas switching. A slight delay of the gas concentration compared to the pressure drop is believed to be caused by gas back-mixing. It is noted that, during these gaseous fuel tests before any use of K-charcoal or Na-charcoal, no defluidization/agglomeration was found for braunite.

4.1.3. Reaction with Solid Fuels. Using charcoal, K-charcoal, or Na-charcoal as solid fuel, typical reduction periods are shown in Figure 8. In the case of charcoal, the addition of solid fuel initially led to a short and small peak of CH_4 from the residual volatiles, while CO and H_2 from steam gasification are seen to gradually decrease. The main gas detected, however, is CO_2.

https://doi.org/10.1021/acs.energyfuels.2c00553
Energy Fuels XXXX, XXX, XXX−XXX

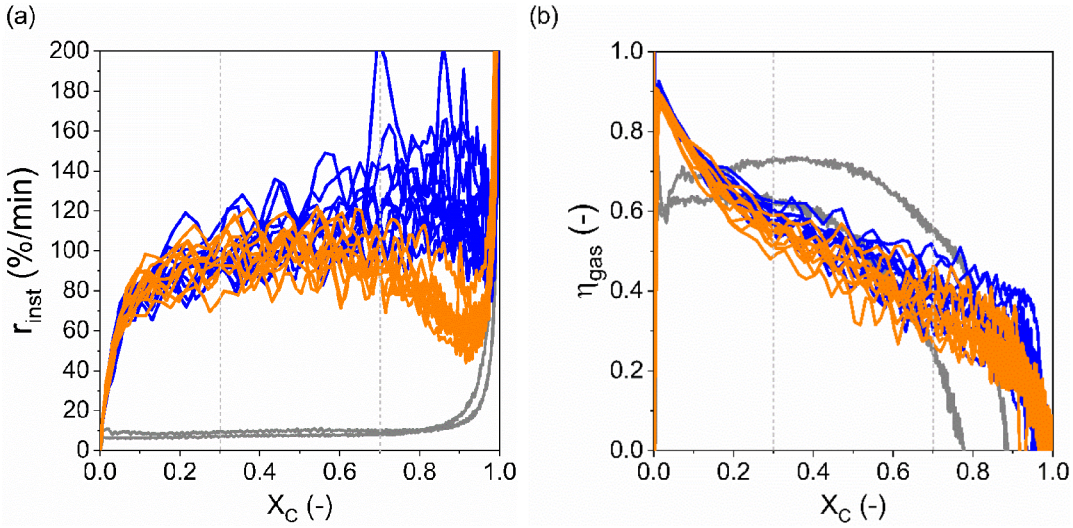

Figure 9. (a) Instantaneous rate of char gasification and (b) gas conversion, as a function of carbon conversion for charcoal (gray lines), K-charcoal (blue lines), and Na-charcoal (orange lines). Charcoal, cycles 7 and 8; K-charcoal, cycles 24−38; and Na-charcoal, cycles 23−37.

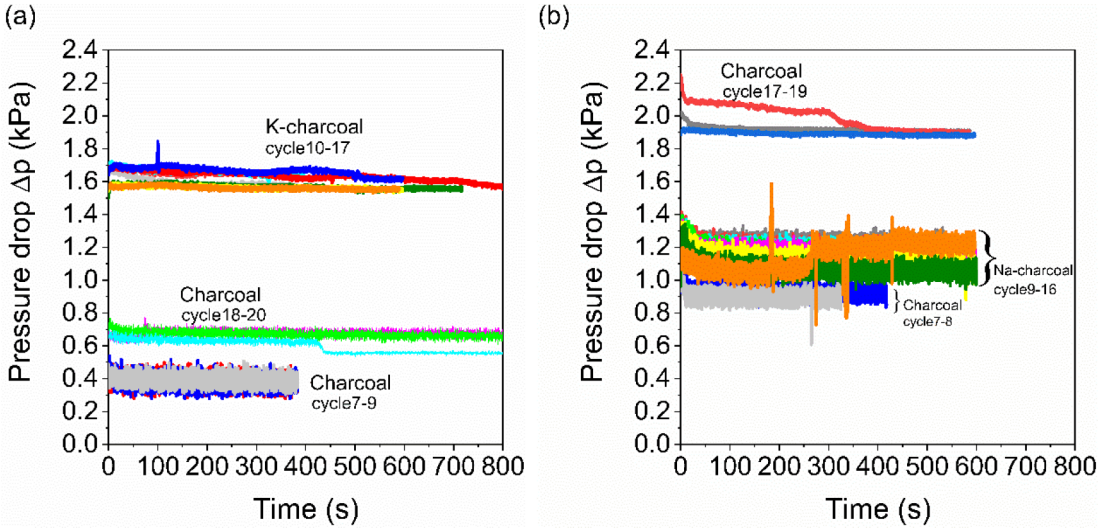

Figure 10. Pressure drop over the reactor as a function of the reaction time during the oxidation periods following (a) charcoal and K-charcoal use and (b) charcoal and Na-charcoal use.

Thus, most of the CO and H_2 intermediates reacted with braunite to CO_2 and H_2O. Unconverted H_2 has a higher concentration than CO, although the former usually has a higher reactivity than the latter. This can be explained by the water−gas shift (WGS) reaction, which converts part of CO and H_2O to CO_2 and H_2 in steam-rich conditions. Complete conversion of charcoal takes around 15 min and has a long tail of CO_2, H_2, and CO concentrations. As the fuel was changed to K-charcoal and Na-charcoal, the char gasification is much faster (i.e., around 5 and 8 min are sufficient for complete conversion), which is a result of the catalytic effects of K and Na.[73,74] Consequently, the concentrations of CO_2, CO, and H_2 for K-charcoal and Na-charcoal are significantly higher than for charcoal. The big pressure drop fluctuations were caused by the steam injection.

4.2. Char Gasification Rate and Gas Conversion. The enhancement of char gasification, seen with K-charcoal or Na-charcoal, is demonstrated in Figure 9a using the instantaneous gasification rate as a function of carbon conversion. In the initial and final carbon conversion (i.e., $X_C \approx 0-0.1$ and 0.9−1.0), the fluctuations are believed to be caused by the low gas concentration and the calculation method (see eq 11). Thus, the instantaneous gasification rate in the range of $X_C = 0.3-0.7$ is used to compare different fuels, similar to previous works.[75,76] In the case of charcoal, the instantaneous gasification rate was around 10%/min within X_C = 0.3−0.7 for the two cycles, whereas the rate for K-charcoal and Na-charcoal was 10 and 9 times higher, i.e., around 100 and 90%/min, respectively. Although the char gasification was greatly improved by catalysis of K and Na, the gas conversion is similar to charcoal (see Figure 9b). For charcoal, K-charcoal, and Na-charcoal, the gas conversion was similar at about 0.4−0.6 when the carbon conversion was X_C = 0.3−0.7. This means that the contact between the gasification products (CO and H_2) and the bed is similar for all three fuels, regardless of the impregnation with alkalis.

4.3. Partial Defluidization and Agglomeration. *4.3.1. Pressure Drop and Fluctuation.* The bed fluidization was monitored by the fluctuations in the pressure drop over the reactor, as shown in Figure 10. Here, the pressure drop during oxidation periods is presented. This is because the reducing

https://doi.org/10.1021/acs.energyfuels.2c00553
Energy Fuels XXXX, XXX, XXX−XXX

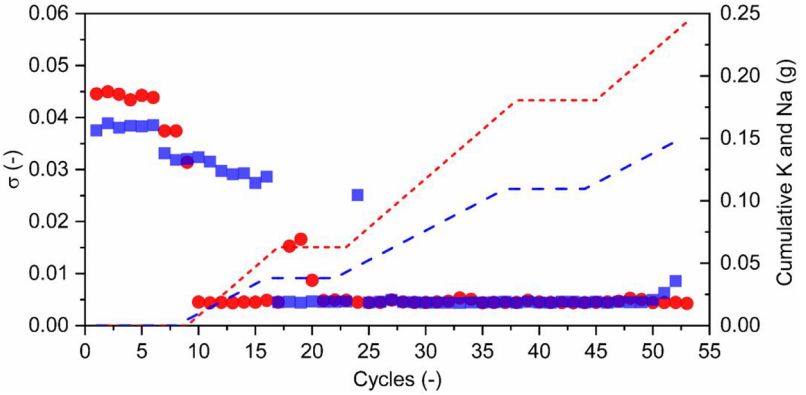

Figure 11. Amplitude of pressure drop fluctuations (K-charcoal, red circles; Na-charcoal, blue squares) and calculated cumulative amount of K (red short dashed line) and Na (blue long dashed line) in braunite as a function of the cycle number.

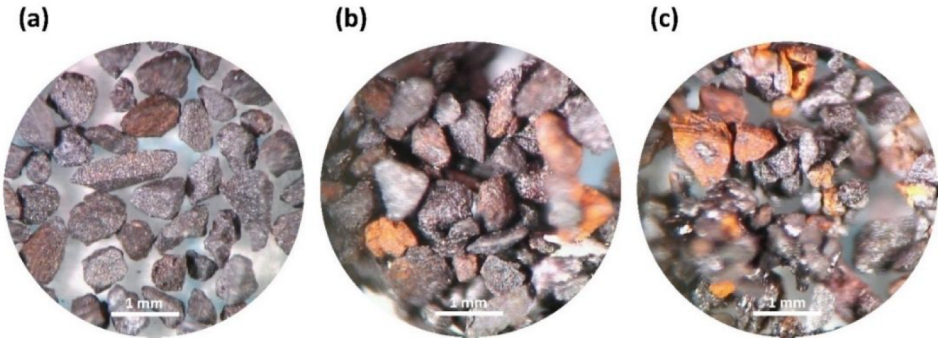

Figure 12. Light microscopic images of (a) fresh, (b) K-final, and (c) Na-final braunite.

periods with solid fuel addition cannot be used as a result of the periodic fluctuations caused by steam injection (cf. Figure 8). In the case of charcoal, before any tests with K-charcoal or Na-charcoal, there was no defluidization/agglomeration in the bed. This was confirmed by the observed well-dispersed bed particles in the cooled reactor after cycle 9 for the K-charcoal series and cycle 8 for the Na-charcoal series. Thus, the pressure fluctuation in the oxidation step of the first charcoal use is considered as a reference, i.e., to show the fluctuations in the absence of agglomeration and defluidization. In Figure 10, charcoal shows a pressure fluctuation of around 0.2 kPa, i.e., from 0.3 to 0.5 kPa in Figure 10a and from 0.8 to 1.0 kPa in Figure 10b. The different ranges for these two cases could be a result of using different reactor tubes, i.e., one tube for K-charcoal and another one for Na-charcoal, which may have a different porosity in the gas distributor. In Figure 10a, the pressure drop fluctuations decreased to below 0.05 kPa when the fuel was changed to K-charcoal in cycles 10−17. The increased pressure drop for K-charcoal compared to charcoal is believed to be a result of partial blockage in the gas distributor, i.e., the porous plate constituting the bottom of the fluidized bed. Much lower pressure fluctuations are seen already in cycle 10 in the case of K-charcoal. Because the bed can freely flow out from the reactor after being cooled, the low-pressure fluctuation suggests a partial defluidization of the bed. This agrees with the observation of a small amount of aggregates of agglomerated particles after cycle 17, whereas most of the particles were not agglomerated. Therefore, partial agglomeration of particles has occurred already in the first several cycles with K-charcoal, indicating a quick agglomeration. The partial defluidization with Na-charcoal is different from K-charcoal (see Figure 10b). Using Na-charcoal, the pressure drop increased gradually in cycles because of pore blockage of the gas distributor. The fluctuations were always at around 0.2 kPa for charcoal in cycles 7 and 8 and Na-charcoal in cycles 9−16. The fluctuations became low, around 0.05 kPa, in cycles 17−19, and this is a bit higher than 0.01 kPa, which was obtained in a fully defluidized bed.[52] Again, the partial defluidization in the case of Na-charcoal agrees with the observation of several small blocks between particles after cycle 16.

Figure 11 shows the amplitude of pressure drop fluctuations σ and the calculated cumulative amount of K and Na injected as a function of cycles for the two series of experiments. In cycles 1−6 with CH_4, the fluctuation amplitude was at 0.037−0.045 for K-charcoal and Na-charcoal series, and this indicates good fluidization. The amplitude of fluctuation in the cycles with charcoal, i.e., cycles 7−9 for the K-charcoal series and cycles 7 and 8 for the Na-charcoal series, also indicates good fluidization because the amplitude is similar or reasonably close to that of CH_4 experiments. However, afterward, an abrupt drop of the fluctuation amplitude was observed for K-charcoal. After cycle 10, which was the first cycle with K-charcoal, the amplitude was usually less than 0.01. In the case of Na-charcoal, the fluctuation amplitude was 0.025−0.032 in cycles 9−16 using Na-charcoal. However, this was decreased to less than 0.01 after cycle 17. Cycle 10 in the K-charcoal series corresponds to 0.00798 g of K addition, and cycle 17 in the Na-charcoal series corresponds to 0.03806 g of Na addition. The low amplitudes of pressure fluctuation coincide with several observed agglomerates of bed particles after cooling the reactor. After cycle 10 for the K-charcoal series and cycle 17 for the Na-charcoal series, the fluctuation amplitude was relatively stable at around 0.005. In

https://doi.org/10.1021/acs.energyfuels.2c00553
Energy Fuels XXXX, XXX, XXX−XXX

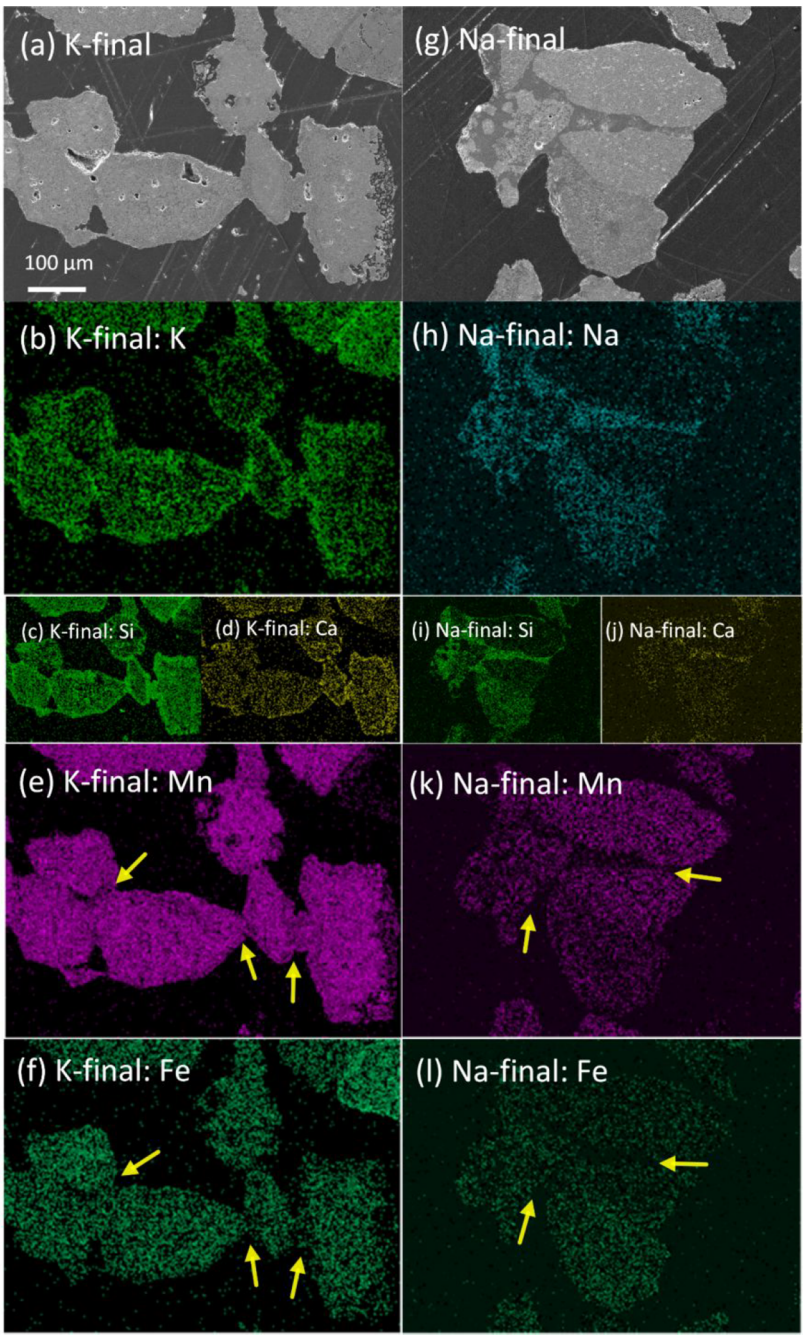

Figure 13. SEM−EDX analyses of the cross section of (a−f) K-final braunite particles and (g−l) Na-final braunite particles. K, Na, Si, Ca, Mn, and Fe elements on the cross section of particles are presented for evaluation and comparison. The yellow arrows indicate the bridges/gaps between particles formed because of partial agglomeration.

addition, K-charcoal can lead to partial defluidization and partial agglomeration faster than Na-charcoal, i.e., start from cycle 10 versus start from cycle 17.

4.3.2. Morphology of Braunite. 4.3.2.1. Light Microscope. Light microscopic images of fresh, K-final, and Na-final braunite samples are described in Figure 12. As observed, some particles have different colors compared to the other particles in the fresh sample, i.e., brown and gray, indicating uneven component distribution in braunite. Slight changes of the color in the K-final and Na-final samples compared to the fresh sample were also noticed. The fresh particles were well-dispersed without agglomerates found. In the case of K-final and Na-final samples, some particles have molten surfaces and were stuck together. This demonstrates the partial agglomeration in K-final and Na-final samples, and the agglomeration is in the soft form; i.e., the agglomerated particles can be separated with fingers. Hard agglomeration, i.e., big blocks that are hard to break, is absent for braunite.

4.3.2.2. SEM−EDX: Agglomeration and K, Na, Si, and Ca Distribution. In fresh braunite, Mn and Fe are distributed evenly and are well-separated among different particles, while extremely low K and Na were detected (not shown here). Agglomerated particles were further studied in SEM−EDX analysis, as seen in Figure 13. The K-final and Na-final samples have bridges between particles (see, e.g., panels a and g of Figure 13). Elemental analysis by SEM−EDX confirmed the accumulation

https://doi.org/10.1021/acs.energyfuels.2c00553
Energy Fuels XXXX, XXX, XXX−XXX

of K and Na in the used particles with K-charcoal and Na-charcoal. The K element was found more on the surface of particles, forming a core−shell-like structure, as seen in Figure 13b, whereas Na is more in phases connecting the particles, seen in Figure 13h. In addition, K shows a higher presence throughout the particle than Na, and this indicates faster diffusion of potassium into the oxygen carrier particles than sodium.[77] Elements of Si and Ca also have a tendency to accumulate on surfaces and bridges (see panels c, d, i, and j of Figure 13). In conventional fluidized bed combustion, a similar accumulation of K, Si, and Ca is observed for agglomerated bed particles.[53,78] Usually, these elements stick on the particles and form initial layers on the surface of bed particles. These layers grow thicker as more ash is introduced and finally develop sticky components, which can glue bed particles together to form agglomerates. Another mechanism for the formation of agglomerates is the direct interaction of these elements with the bed material, which lowers the melting point of the particles and forms molten interfaces, which lead to agglomeration. Similar mechanisms of bed agglomeration are also relevant for sodium.[79] Our observations of the distribution of K, Na, Si, and Ca in the bridges agree well with those in the literature of conventional fluidized bed combustion,[53,78,80] and this suggests K−Si−Ca and Na−Si−Ca systems might be responsible for the formation of agglomerates in braunite.

4.3.2.3. SEM−EDX: Behavior of Mn and Fe. As seen in Figure 13, both Mn and Fe elements are well-represented in the K-final and Na-final samples. The difference lies in the bridges between agglomerated particles. In the case of K-final braunite, both Mn and Fe were observed in the bridges, suggesting that the particles have been melted to some extent during the formation of agglomerates. However, in the agglomerate bridges of Na-final braunite samples, Mn and Fe are almost absent; thus, the bridges appear as gaps in panels k and l of Figure 13. Instead, Na, Si, and Ca are dominant in these bridges, as seen in panels h−j of Figure 13. This phenomenon suggests that Mn and Fe may not contribute to the agglomeration of the Na-final braunite sample, in contrast to the K-final sample. Therefore, the mechanism of agglomerate formation in the K-charcoal and Na-charcoal series of experiments is different. In the K-charcoal series, agglomerates appear to form in a manner of particle surface melting, which makes particles stick together. Thus, Mn and Fe were found in the bridges between agglomerated K-final braunite particles, and this could be classified to melt-induced agglomeration.[80] On the contrary, for the Na-final sample, Mn or Fe was not found between particles and Na, Si, and Ca in the bridges constitute the new components, which glue particles together to form agglomerates, i.e., coating-induced agglomeration.[80] This again agrees well with the studies for conventional fluidized bed combustion, discussed in the section above.

4.4. Retention of K and Na in Braunite. In Figure 14, the amount of K and Na measured in the braunite middle and final samples is compared to the theoretical cumulative alkali addition with fuel. Both data were calculated on the basis of the ICP−OES analyses of the samples. The alkalis presented in the bed samples were usually referred to alkali retention in the oxygen carrier.[56] Thus, most Na introduced is retained in braunite, whereas less than half of K is retained, showing a lower affinity of K with the braunite bed. This indicates a higher tendency of the Na interaction with braunite compared to K. Remaining K and Na could either have left the reactor with the gas or reacted with the walls of the quartz reactor. Total added K and Na was 0.24 and 0.16 g, which is 0.8−1.2% of the braunite weight. In the final

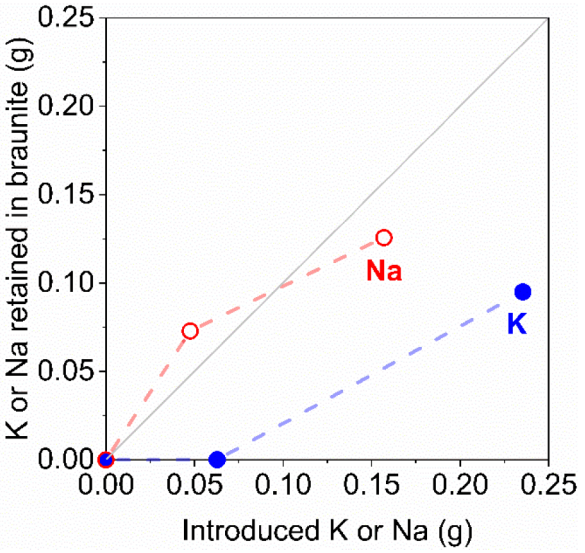

Figure 14. Retention of K and Na in braunite as a function of the cumulative amount of K and Na introduced with the solid fuels.

samples, around 40% of K and 80% of Na added were found in the braunite oxygen carrier. The retention of K and Na could be a result of agglomeration, meaning that the alkalis can stay in the agglomerates mainly on the particle surface, as seen in the SEM−EDX results. In addition, alkalis can diffuse into the particle through the pores in the particle, forming a stable phase. Nevertheless, no such alkali-based phases were found through XRD analysis, as seen in Figure 2. However, this could be because the absolute amount of alkali retention is low or the phase is in the amorphous form and cannot be identified by the XRD technique.

4.5. Reactivity of Fresh and Used Braunite. The fresh and used oxygen carrier samples were tested with CH_4 and syngas to evaluate the reactivity with CH_4, CO, and H_2. The rate constant as a function of the mass-based oxygen carrier conversion is shown in Figure 15a. In general, the rate constant decreases gradually as the oxygen carrier is more reduced, i.e., a lower rate constant at a lower value of conversion. CH_4 has the lowest reactivity, with the rate constant varying in the range of 0.03−0.1 $L_n\ kg^{-1}\ s^{-1}$ and the conversion changing between 1 and 0.997. In the case of syngas, the rate constant for CO and H_2 is much higher than that for CH_4 and has a wider range of oxygen carrier conversion, i.e., from 1 to 0.965. Further, the rate constant for H_2 is in the range of 4.5−8.7 $L_n\ kg^{-1}\ s^{-1}$, which is higher than that for CO, i.e., 1.5−5.1 $L_n\ kg^{-1}\ s^{-1}$. Figure 15b shows the rate constant in cycles with CH_4 and syngas. The rates at $\omega = 0.998$ with CH_4 and 0.98 with syngas are plotted for fresh, K-final, and Na-final braunite samples.[71,81] In the case of reacting with CH_4, fresh and used braunites have very similar rate constants in cycles and the rate was quite stable. The reactivity of fresh braunite with CO had a slight decrease until the fifth cycle while a small increase for K-final and Na-final with CO. A small increase of the rate constant with H_2 was found for the fresh and used samples in the first 3 cycles and then became stable. However, because the difference in the rate constant is small, the reactivities of fresh, K-final, and Na-final braunite samples are similar, although the materials have accumulated K or Na and undergone partial defluidization and partial agglomeration.

https://doi.org/10.1021/acs.energyfuels.2c00553
Energy Fuels XXXX, XXX, XXX−XXX

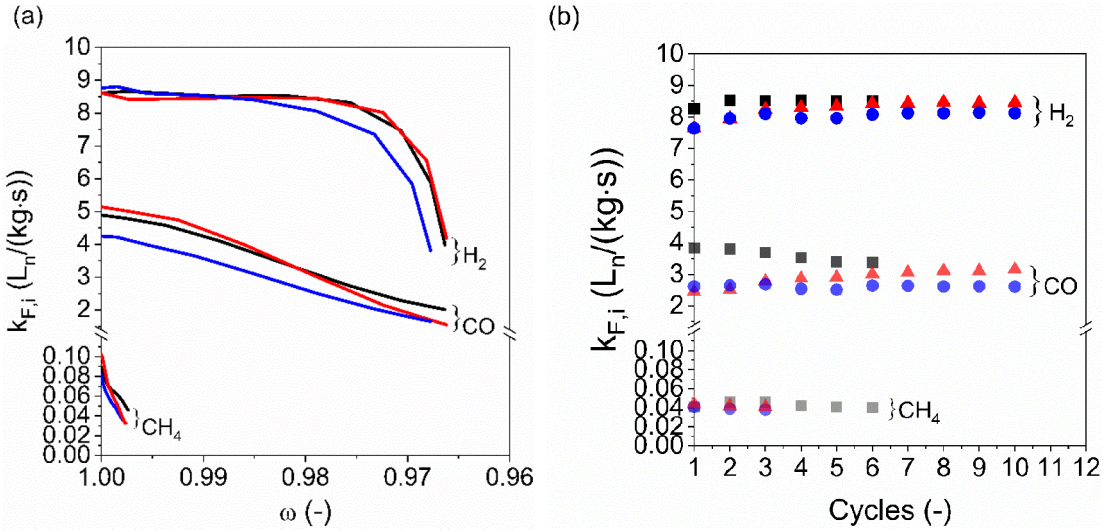

Figure 15. (a) Rate constant for CH_4, CO, and H_2 versus mass-based oxygen carrier conversion for fresh (black lines), K-final (blue lines), and Na-final (red lines). Fresh braunite data are from cycle 6 with CH_4 in the K-charcoal series and from cycle 6 with syngas; K-final data are from cycles 45 and 10 with syngas; and Na-final data are from cycles 44 and 10 with syngas. (b) Rate constant versus cycle number with CH_4 and syngas for fresh (black squares), K-final (blue circles), and Na-final (red triangles) samples. Data are from ω = 0.998 with CH_4 and 0.98 with syngas.

5. CONCLUSION

The interaction of K and Na with a braunite ore oxygen carrier was studied in a batch fluidized bed reactor using charcoal and charcoal impregnated with either K_2CO_3 or Na_2CO_3 as well as gaseous fuels (CH_4 and syngas). The presence of K or Na in the solid fuel resulted in a char gasification rate of 9−10 times that of charcoal, demonstrating strong alkali catalytic effects. Partial agglomeration and partial defluidization of the braunite bed were detected for both K-charcoal and Na-charcoal, with an earlier partial agglomeration/defluidization for K-charcoal. K, Na, Si, and Ca were enriched on the particle surfaces as well as in the bridges among agglomerated particles; thus, the K−Si−Ca and Na−Si−Ca systems can be assumed to be responsible for the agglomeration. No Fe or Mn was found in the bridges causing agglomerates of Na-charcoal used braunite particles, whereas they were present in the case of K-charcoal used samples. Thus, different mechanisms explain agglomerations in K-charcoal and Na-charcoal cases. Presumably, oxygen carrier surface melting for K-charcoal and oxygen carrier particle gluing from possible newly formed components for Na-charcoal are the mechanisms of agglomeration. K and Na added were partly retained in braunite, with K having around 40% retention and Na having around 80% retention. Total added K and Na was 0.8−1.2% of braunite. Despite partial agglomeration and alkali retention, the reactivity of braunite with CH_4, CO, and H_2 was essentially the same as that of the fresh oxygen carrier.

AUTHOR INFORMATION

Corresponding Author

Daofeng Mei − *Division of Energy Technology, Department of Space, Earth and Environment, Chalmers University of Technology, 41296 Gothenburg, Sweden; College of Engineering, Huazhong Agricultural University, Wuhan, Hubei 430070, People's Republic of China;* orcid.org/0000-0001-8597-1903; Phone: +46-317-725-244; Email: daofeng.mei@chalmers.se

Authors

Anders Lyngfelt − *Division of Energy Technology, Department of Space, Earth and Environment, Chalmers University of Technology, 41296 Gothenburg, Sweden;* orcid.org/0000-0002-9561-6574

Henrik Leion − *Department of Chemistry and Chemical Engineering, Chalmers University of Technology, 41293 Gothenburg, Sweden;* orcid.org/0000-0002-9716-2553

Carl Linderholm − *Division of Energy Technology, Department of Space, Earth and Environment, Chalmers University of Technology, 41296 Gothenburg, Sweden*

Tobias Mattisson − *Division of Energy Technology, Department of Space, Earth and Environment, Chalmers University of Technology, 41296 Gothenburg, Sweden;* orcid.org/0000-0003-3942-7434

Complete contact information is available at: https://pubs.acs.org/10.1021/acs.energyfuels.2c00553

Notes

The authors declare no competing financial interest.

ACKNOWLEDGMENTS

This work was carried out under the project funded by the Swedish Research Council (47223126), with special thanks to Fredrik Hildor for his support on cross-section sample preparation, Amir H. Soleimanisalim and Victor Purnomo for their support on SEM−EDX and XRD characterizations, and Jessica Malene Bohwalli for providing the charcoal.

NOMENCLATURE

CCS = carbon capture and storage
CLC = chemical looping combustion
CLOU = chemical looping with oxygen uncoupling
fresh = fresh braunite oxygen carrier before any experimental tests
ICP−OES = inductively coupled plasma optical emission spectrometry
ICSD = Inorganic Crystal Structure Database

https://doi.org/10.1021/acs.energyfuels.2c00553
Energy Fuels XXXX, XXX, XXX−XXX

$k_{F,i}$ = reaction rate constant of the oxygen carrier with gas i (i = CH_4, CO, or H_2) (L_n kg^{-1} s^{-1})
K-charcoal = charcoal impregnated with K_2CO_3
K-final = braunite oxygen carrier sample from the final cycle with K-charcoal
K-middle = braunite oxygen carrier sample from the middle cycles with K-charcoal
$m_C(t)$ = total mass of carbon leaving the reactor at time t (g)
$m_{C,tot}$ = total mass of carbon measured during the entire reduction with solid fuel (g)
m_{ox} = amount of braunite oxygen carrier used in the experiments (g)
MeO_x = oxygen carrier in the oxidized form
MeO_{x-1} = oxygen carrier in the reduced form
M_C = molar mass of atomic carbon (g/mol)
M_O = molar mass of atomic oxygen (g/mol)
n = nth number of the N pressure drop values
N = number of points used for σ calculation
Na-charcoal = charcoal impregnated with Na_2CO_3
Na-final = braunite oxygen carrier sample from the final cycle with Na-charcoal
Na-middle = braunite oxygen carrier sample from the middle cycles with Na-charcoal
r_{inst} = instantaneous rate of char gasification (%/min)
SEM−EDX = scanning electron microscopy−energy-dispersive X-ray spectroscopy
t = instantaneous reaction time (s)
t_0 = time at the beginning of reduction (s)
V_i = volumetric flow of CH_4 or syngas used for batch reactor tests (L_n/s)
WGS = water−gas shift
x_i = dry gas concentration of gas i (i = CH_4, CO, CO_2, H_2, or O_2)
X_C = carbon conversion in the solid fuels
XRD = X-ray diffraction
Δp = pressure drop over the bed (kPa)
Δp_n = nth pressure drop value (kPa)
Δp_{avg} = average of the N pressure drop values (kPa)
$\gamma_{i,j}$ = gas yield for component i (i = CH_4, CO, and H_2) in the reaction with methane (j = CH_4) or syngas (j = syn)
η_{gas} = gas conversion for solid fuel
σ = amplitude of pressure drop fluctuation
ω_i = mass-based oxygen carrier conversion in the reaction with gas CH_4 (i = CH_4) or syngas (i = syn)
$\dot{n}_{out}$ = molar flow rate of gas passing through the gas analyzer (mol/s)

REFERENCES

(1) United Nations Framework Convention on Climate Change (UNFCCC). *The Paris Agreement*; UNFCCC: Bonn, Germany, 2015; http://unfccc.int/paris_agreement/items/9485.php.
(2) Intergovernmental Panel on Climate Change (IPCC). *Special Report: Global Warming of 1.5 °C. Summary for Policymakers*; IPCC: Geneva, Switzerland, 2018; https://www.ipcc.ch/sr15/chapter/summary-for-policymakers/.
(3) International Energy Agency (IEA). *World Energy Outlook 2017, Executive Summary*; IEA: Paris, France, 2017.
(4) Boot-Handford, M. E.; Abanades, J. C.; Anthony, E. J.; Blunt, M. J.; Brandani, S.; Mac Dowell, N.; Fernández, J. R.; Ferrari, M.-C.; Gross, R.; Hallett, J. P.; Haszeldine, R. S.; Heptonstall, P.; Lyngfelt, A.; Makuch, Z.; Mangano, E.; Porter, R. T. J.; Pourkashanian, M.; Rochelle, G. T.; Shah, N.; Yao, G. J.; Fennell, P. S. Carbon capture and storage update. *Energy Environ. Sci.* **2014**, *7*, 130−189.
(5) Mukherjee, S.; Kumar, P.; Yang, A.; Fennell, P. Energy and exergy analysis of chemical looping combustion technology and comparison with pre-combustion and oxy-fuel combustion technologies for CO_2 capture. *J. Environ. Chem. Eng.* **2015**, *3* (3), 2104−2114.
(6) Lyngfelt, A.; Leckner, B.; Mattisson, T. A fluidized-bed combustion process with inherent CO_2 separation: Application of chemical-looping combustion. *Chem. Eng. Sci.* **2001**, *56* (10), 3101−3113.
(7) Adánez, J.; Abad, A.; Mendiara, T.; Gayán, P.; de Diego, L. F.; García-Labiano, F. Chemical looping combustion of solid fuels. *Prog. Energy Combust. Sci.* **2018**, *65*, 6−66.
(8) Fan, J.; Zhu, L.; Hong, H.; Jiang, Q.; Jin, H. A thermodynamic and environmental performance of in-situ gasification of chemical looping combustion for power generation using ilmenite with different coals and comparison with other coal-driven power technologies for CO2 capture. *Energy* **2017**, *119*, 1171−1180.
(9) Mukherjee, S.; Kumar, P.; Yang, A.; Fennell, P. Energy and exergy analysis of chemical looping combustion technology and comparison with pre-combustion and oxy-fuel combustion technologies for CO_2 capture. *J. Environ. Chem. Eng.* **2015**, *3* (3), 2104−2114.
(10) Mattisson, T.; Keller, M.; Linderholm, C.; Moldenhauer, P.; Rydén, M.; Leion, H.; Lyngfelt, A. Chemical-looping technologies using circulating fluidized bed systems: Status of development. *Fuel Process. Technol.* **2018**, *172*, 1−12.
(11) Lyngfelt, A.; Kronberger, B.; Adánez, J.; Morin, J.-X.; Hurst, P. GRACE project. Development of oxygen carrier particles for chemical-looping combustion. Design and operation of a 10 kW chemical-looping combustor. *Proceedings of the 7th International Conference on Greenhouse Gas Control Technologies (GHGT-7)*; Vancouver, British Columbia, Canada, Sept 5−9, 2004.
(12) Tang, M.; Xu, L.; Fan, M. Progress in oxygen carrier development of methane-based chemical-looping reforming: A review. *Appl. Energy* **2015**, *151*, 143−156.
(13) Lyngfelt, A. Chemical Looping Combustion: Status and Development Challenges. *Energy Fuels* **2020**, *34* (8), 9077−9093.
(14) Rydén, M.; Moldenhauer, P.; Mattisson, T.; Lyngfelt, A.; Younes, M.; Niass, T.; Fadhel, B.; Ballaguet, J.-P. Chemical-Looping Combustion with Liquid Fuels. *Energy Procedia* **2013**, *37*, 654−661.
(15) Lyngfelt, A. Chemical-looping combustion of solid fuels—Status of development. *Appl. Energy* **2014**, *113*, 1869−1873.
(16) Lyngfelt, A.; Johansson, M.; Mattisson, T. Chemical-looping combustion—Status of development. *Proceedings of the 9th International Conference on Circulating Fluidized Beds (CFB-9)*; Hamburg, Germany, May 13−16, 2008.
(17) Mattisson, T.; Lyngfelt, A.; Leion, H. Chemical-looping with oxygen uncoupling for combustion of solid fuels. *Int. J. Greenhouse Gas Control* **2009**, *3* (1), 11−19.
(18) Imtiaz, Q.; Hosseini, D.; Müller, C. R. Review of Oxygen Carriers for Chemical Looping with Oxygen Uncoupling (CLOU): Thermodynamics, Material Development, and Synthesis. *Energy Technol.* **2013**, *1* (11), 633−647.
(19) Mattisson, T. Materials for Chemical-Looping with Oxygen Uncoupling. *ISRN Chem. Eng.* **2013**, *2013*, 1−19.
(20) Mendiara, T.; García-Labiano, F.; Abad, A.; Gayán, P.; de Diego, L. F.; Izquierdo, M. T.; Adánez, J. Negative CO_2 emissions through the use of biofuels in chemical looping technology: A review. *Appl. Energy* **2018**, *232*, 657−684.
(21) Rydén, M.; Lyngfelt, A.; Langørgen, Ø.; Larring, Y.; Brink, A.; Teir, S.; Havåg, H.; Karmhagen, P. Negative CO_2 Emissions with Chemical-Looping Combustion of Biomass—A Nordic Energy Research Flagship Project. *Energy Procedia* **2017**, *114*, 6074−6082.
(22) Mendiara, T.; Pérez-Astray, A.; Izquierdo, M. T.; Abad, A.; de Diego, L. F.; García-Labiano, F.; Gayán, P.; Adánez, J. Chemical Looping Combustion of different types of biomass in a 0.5 kW_{th} unit. *Fuel* **2018**, *211*, 868−875.
(23) Shen, L.; Wu, J.; Xiao, J.; Song, Q.; Xiao, R. Chemical-Looping Combustion of Biomass in a 10 kW_{th} Reactor with Iron Oxide As an Oxygen Carrier. *Energy Fuels* **2009**, *23* (5), 2498−2505.

https://doi.org/10.1021/acs.energyfuels.2c00553
Energy Fuels XXXX, XXX, XXX−XXX

(24) Schmitz, M.; Linderholm, C. Chemical looping combustion of biomass in 10- and 100-kW pilots—Analysis of conversion and lifetime using a sintered manganese ore. *Fuel* **2018**, *231*, 73−84.
(25) Mei, D.; Linderholm, C.; Lyngfelt, A. Performance of an oxy-polishing step in the 100 kW_{th} chemical looping combustion prototype. *Chem. Eng. J.* **2021**, *409*, 128202.
(26) Mei, D.; Soleimanisalim, A. H.; Linderholm, C.; Lyngfelt, A.; Mattisson, T. Reactivity and lifetime assessment of an oxygen releasable manganese ore with biomass fuels in a 10 kW_{th} pilot rig for chemical looping combustion. *Fuel Process. Technol.* **2021**, *215*, 106743.
(27) Penthor, S.; Fuchs, J.; Benedikt, F.; Schmid, J. C.; Mauerhofer, A. M.; Mayer, K.; Hofbauer, H. First results from an 80 kW dual fluidized bed pilot unit for solid fuels at TU Wien. *Proceedings of the 5th International Conference on Chemical Looping*; Park City, UT, Sept 24−27, 2018.
(28) Pikkarainen, T.; Hiltunen, I.; Teir, S. Piloting of bio-CLC for BECCS *Proceedings of the 4th International Conference on Chemical Looping*; Nanjing, China, Sept 26−28, 2016.
(29) Vilches, T. B.; Lind, F.; Rydén, M.; Thunman, H. Experience of more than 1000 h of operation with oxygen carriers and solid biomass at large scale. *Appl. Energy* **2017**, *190*, 1174−1183.
(30) Lyngfelt, A.; Brink, A.; Langørgen, Ø.; Mattisson, T.; Rydén, M.; Linderholm, C. 11,000 h of chemical-looping combustion operation—Where are we and where do we want to go? *Int. J. Greenhouse Gas Control* **2019**, *88*, 38−56.
(31) Rubel, A.; Zhang, Y.; Neathery, J. K.; Liu, K. Comparative Study of the Effect of Different Coal Fly Ashes on the Performance of Oxygen Carriers for Chemical Looping Combustion. *Energy Fuels* **2012**, *26* (6), 3156−3161.
(32) Siriwardane, R.; Tian, H.; Richards, G.; Simonyi, T.; Poston, J. Chemical-Looping Combustion of Coal with Metal Oxide Oxygen Carriers. *Energy Fuels* **2009**, *23* (8), 3885−3892.
(33) Zevenhoven, M.; Yrjas, P.; Skrifvars, B.-J.; Hupa, M. Characterization of Ash-Forming Matter in Various Solid Fuels by Selective Leaching and Its Implications for Fluidized-Bed Combustion. *Energy Fuels* **2012**, *26* (10), 6366−6386.
(34) Sutton, D.; Kelleher, B.; Ross, J. R. H. Review of literature on catalysts for biomass gasification. *Fuel Process. Technol.* **2001**, *73* (3), 155−173.
(35) McKee, D. W. Mechanisms of the alkali metal catalysed gasification of carbon. *Fuel* **1983**, *62* (2), 170−175.
(36) Keller, M.; Leion, H.; Mattisson, T. Mechanisms of Solid Fuel Conversion by Chemical-Looping Combustion (CLC) using Manganese Ore: Catalytic Gasification by Potassium Compounds. *Energy Technol.* **2013**, *1* (4), 273−282.
(37) Scala, F.; Chirone, R. An SEM/EDX study of bed agglomerates formed during fluidized bed combustion of three biomass fuels. *Biomass Bioenergy* **2008**, *32* (3), 252−266.
(38) Chirone, R.; Miccio, F.; Scala, F. Mechanism and prediction of bed agglomeration during fluidized bed combustion of a biomass fuel: Effect of the reactor scale. *Chem. Eng. J.* **2006**, *123* (3), 71−80.
(39) Morris, J. D.; Daood, S. S.; Chilton, S.; Nimmo, W. Mechanisms and mitigation of agglomeration during fluidized bed combustion of biomass: A review. *Fuel* **2018**, *230*, 452−473.
(40) Saidur, R.; Abdelaziz, E. A.; Demirbas, A.; Hossain, M. S.; Mekhilef, S. A review on biomass as a fuel for boilers. *Renewable Sustainable Energy Rev.* **2011**, *15* (5), 2262−2289.
(41) Åbo Akademi University. *Åbo Akademi University Chemical Fractionation Database*; Åbo Akademi University: Turku, Finland, 2022; https://web.abo.fi/fak/tkf/ook/bransle/.
(42) Grimm, A.; Skoglund, N.; Boström, D.; Boman, C.; Öhman, M. Influence of Phosphorus on Alkali Distribution during Combustion of Logging Residues and Wheat Straw in a Bench-Scale Fluidized Bed. *Energy Fuels* **2012**, *26* (5), 3012−3023.
(43) Lane, D. J.; Zevenhoven, M.; Ashman, P. J.; van Eyk, P. J.; Hupa, M.; de Nys, R.; Lewis, D. M. Algal Biomass: Occurrence of the Main Inorganic Elements and Simulation of Ash Interactions with Bed Material. *Energy Fuels* **2014**, *28* (7), 4622−4632.
(44) Piotrowska, P.; Grimm, A.; Skoglund, N.; Boman, C.; Öhman, M.; Zevenhoven, M.; Boström, D.; Hupa, M. Fluidized-Bed Combustion of Mixtures of Rapeseed Cake and Bark: The Resulting Bed Agglomeration Characteristics. *Energy Fuels* **2012**, *26* (4), 2028−2037.
(45) Nunes, L. J. R.; Matias, J. C. O.; Catalão, J. P. S. Biomass combustion systems: A review on the physical and chemical properties of the ashes. *Renewable Sustainable Energy Rev.* **2016**, *53*, 235−242.
(46) Lyngfelt, A.; Leckner, B. A 1000 MW_{th} boiler for chemical-looping combustion of solid fuels—Discussion of design and costs. *Appl. Energy* **2015**, *157*, 475−487.
(47) Bao, J.; Li, Z.; Cai, N. Promoting the Reduction Reactivity of Ilmenite by Introducing Foreign Ions in Chemical Looping Combustion. *Ind. Eng. Chem. Res.* **2013**, *52* (18), 6119−6128.
(48) Bao, J.; Li, Z.; Cai, N. Interaction between iron-based oxygen carrier and four coal ashes during chemical looping combustion. *Appl. Energy* **2014**, *115*, 549−558.
(49) Azis, M. M.; Leion, H.; Jerndal, E.; Steenari, B.-M.; Mattisson, T.; Lyngfelt, A. The Effect of Bituminous and Lignite Ash on the Performance of Ilmenite as Oxygen Carrier in Chemical-Looping Combustion. *Chem. Eng. Technol.* **2013**, *36* (9), 1460−1468.
(50) Störner, F.; Hildor, F.; Leion, H.; Zevenhoven, M.; Hupa, L.; Rydén, M. Potassium Ash Interactions with Oxygen Carriers Steel Converter Slag and Iron Mill Scale in Chemical-Looping Combustion of Biomass—Experimental Evaluation Using Model Compounds. *Energy Fuels* **2020**, *34* (2), 2304−2314.
(51) Staničić, I.; Andersson, V.; Hanning, M.; Mattisson, T.; Backman, R.; Leion, H. Combined manganese oxides as oxygen carriers for biomass combustion—Ash interactions. *Chem. Eng. Res. Des.* **2019**, *149*, 104−120.
(52) Purnomo, V.; Yilmaz, D.; Leion, H.; Mattisson, T. Study of defluidization of iron- and manganese-based oxygen carriers under highly reducing conditions in a lab-scale fluidized-bed batch reactor. *Fuel Process. Technol.* **2021**, *219*, 106874.
(53) Niu, Y.; Tan, H.; Hui, S. Ash-related issues during biomass combustion: Alkali-induced slagging, silicate melt-induced slagging (ash fusion), agglomeration, corrosion, ash utilization, and related countermeasures. *Prog. Energy Combust. Sci.* **2016**, *52*, 1−61.
(54) Zevenhoven, M.; Sevonius, C.; Salminen, P.; Lindberg, D.; Brink, A.; Yrjas, P.; Hupa, L. Defluidization of the oxygen carrier ilmenite—Laboratory experiments with potassium salts. *Energy* **2018**, *148*, 930−940.
(55) Gu, H.; Shen, L.; Zhong, Z.; Zhou, Y.; Liu, W.; Niu, X.; Ge, H.; Jiang, S.; Wang, L. Interaction between biomass ash and iron ore oxygen carrier during chemical looping combustion. *Chem. Eng. J.* **2015**, *277*, 70−78.
(56) Gogolev, I.; Linderholm, C.; Gall, D.; Schmitz, M.; Mattisson, T.; Pettersson, J. B. C.; Lyngfelt, A. Chemical-looping combustion in a 100 kW unit using a mixture of synthetic and natural oxygen carriers—Operational results and fate of biomass fuel alkali. *Int. J. Greenhouse Gas Control* **2019**, *88*, 371−382.
(57) Gogolev, I.; Pikkarainen, T.; Kauppinen, J.; Linderholm, C.; Steenari, B.-M.; Lyngfelt, A. Investigation of biomass alkali release in a dual circulating fluidized bed chemical looping combustion system. *Fuel* **2021**, *297*, 120743.
(58) International Organization for Standardization (ISO). *ISO 18134-2:2017. Solid Biofuels—Determination of Moisture Content—Oven Dry Method—Part 2: Total Moisture—Simplified Method*; ISO: Geneva, Switzerland, 2017.
(59) International Organization for Standardization (ISO). *ISO 18122:2015. Solid Biofuels—Determination of Ash Content*; ISO: Geneva, Switzerland, 2015.
(60) International Organization for Standardization (ISO). *ISO 18123:2015. Solid Biofuels—Determination of the Content of Volatile Matter*; ISO: Geneva, Switzerland, 2015.
(61) International Organization for Standardization (ISO). *ISO 16994:2016. Solid Biofuels—Determination of Total Content of Sulfur and Chlorine*; ISO: Geneva, Switzerland, 2016.

https://doi.org/10.1021/acs.energyfuels.2c00553
Energy Fuels XXXX, XXX, XXX−XXX

(62) International Organization for Standardization (ISO). *ISO 16948:2015. Solid Biofuels—Determination of Total Content of Carbon, Hydrogen and Nitrogen*; ISO: Geneva, Switzerland, 2015.
(63) International Organization for Standardization (ISO). *ISO 18125:2017. Solid Biofuels—Determination of Calorific Value*; ISO: Geneva, Switzerland, 2017.
(64) ASTM International. *ASTM D3682-13—Standard Test Method for Major and Minor Elements in Combustion Residues from Coal Utilization Processes*; ASTM International: West Conshohocken, PA, 2013.
(65) Pikkarainen, T.; Hiltunen, I. Chemical looping combustion of solid biomass—Performance of ilmenite and braunite as oxygen carrier materials. *Proceedings of the European Biomass Conference & Exhibition*; Stockholm, Sweden, June 12−15, 2017.
(66) Hellenbrandt, M. The Inorganic Crystal Structure Database (ICSD)—Present and Future. *Crystallogr. Rev.* **2004**, *10* (1), 17−22.
(67) Azimi, G.; Rydén, M.; Leion, H.; Mattisson, T.; Lyngfelt, A. $(Mn_zFe_{1-z})_yO_x$ combined oxides as oxygen carrier for chemical-looping with oxygen uncoupling. *AIChE J.* **2013**, *59* (2), 582−588.
(68) Mei, D.; Abad, A.; Zhao, H.; Adánez, J. Characterization of a sol−gel derived $CuO/CuAl_2O_4$ oxygen carrier for chemical looping combustion (CLC) of gaseous fuels: Relevance of gas−solid and oxygen uncoupling reactions. *Fuel Process. Technol.* **2015**, *133*, 210−219.
(69) Mei, D.; Zhao, H.; Ma, Z.; Zheng, C. Using the Sol−Gel-Derived $CuO/CuAl_2O_4$ Oxygen Carrier in Chemical Looping with Oxygen Uncoupling for Three Typical Coals. *Energy Fuels* **2013**, *27* (5), 2723−2731.
(70) Sundqvist, S.; Khalilian, N.; Leion, H.; Mattisson, T.; Lyngfelt, A. Manganese ores as oxygen carriers for chemical-looping combustion (CLC) and chemical-looping with oxygen uncoupling (CLOU). *J. Environ. Chem. Eng.* **2017**, *5* (3), 2552−2563.
(71) Mei, D.; Soleimanisalim, A. H.; Lyngfelt, A.; Leion, H.; Linderholm, C.; Mattisson, T. Modelling of gas conversion with an analytical reactor model for biomass chemical looping combustion (bio-CLC) of solid fuels. *Chem. Eng. J.* **2022**, *433*, 133563.
(72) Mei, D.; Mendiara, T.; Abad, A.; de Diego, L. F.; García-Labiano, F.; Gayán, P.; Adánez, J.; Zhao, H. Evaluation of Manganese Minerals for Chemical Looping Combustion. *Energy Fuels* **2015**, *29* (10), 6605−6615.
(73) Mei, D.; Mendiara, T.; Abad, A.; de Diego, L. F.; García-Labiano, F.; Gayán, P.; Adánez, J.; Zhao, H. Manganese Minerals as Oxygen Carriers for Chemical Looping Combustion of Coal. *Ind. Eng. Chem. Res.* **2016**, *55* (22), 6539−6546.
(74) Frohn, P.; Arjmand, M.; Azimi, G.; Leion, H.; Mattisson, T.; Lyngfelt, A. On the high-gasification rate of Brazilian manganese ore in chemical-looping combustion (CLC) for solid fuels. *AIChE J.* **2013**, *59* (11), 4346−4354.
(75) Keller, M.; Leion, H.; Mattisson, T.; Lyngfelt, A. Gasification inhibition in chemical-looping combustion with solid fuels. *Combust. Flame* **2011**, *158* (3), 393−400.
(76) Arjmand, M.; Leion, H.; Mattisson, T.; Lyngfelt, A. Investigation of different manganese ores as oxygen carriers in chemical-looping combustion (CLC) for solid fuels. *Appl. Energy* **2014**, *113*, 1883−1894.
(77) Thy, P.; Lesher, C. E.; Jenkins, B. M. Experimental determination of high-temperature elemental losses from biomass slag. *Fuel* **2000**, *79* (6), 693−700.
(78) Grimm, A.; Öhman, M.; Lindberg, T.; Fredriksson, A.; Boström, D. Bed Agglomeration Characteristics in Fluidized-Bed Combustion of Biomass Fuels Using Olivine as Bed Material. *Energy Fuels* **2012**, *26* (7), 4550−4559.
(79) Boström, D.; Skoglund, N.; Grimm, A.; Boman, C.; Öhman, M.; Broström, M.; Backman, R. Ash transformation chemistry during combustion of biomass. *Energy Fuels* **2012**, *26*, 85−93.
(80) Visser, H. J. M.; van Lith, S. C.; Kiel, J. H. A. Biomass Ash-Bed Material Interactions Leading to Agglomeration in FBC. *J. Energy Resour. Technol.* **2008**, *130* (1), 011801.
(81) Berguerand, N. Design and Operation of a 10 kW_{th} Chemical-Looping Combustor for Solid Fuels. Ph.D. Thesis, Chalmers University of Technology, Gothenburg, Sweden, 2009.

https://doi.org/10.1021/acs.energyfuels.2c00553
Energy Fuels XXXX, XXX, XXX−XXX